

Quantum defects of nF_J levels of Cs Rydberg atoms

Jingxu Bai,¹ Rong Song,¹ Jiabei Fan,¹ Yuechun Jiao^{1,2,*}, Jianming Zhao^{1,2,†}, Suotang Jia,^{1,2} and Georg Raithel^{3,‡}

¹State Key Laboratory of Quantum Optics and Quantum Optics Devices, Institute of Laser Spectroscopy, Shanxi University, Taiyuan 030006, China

²Collaborative Innovation Center of Extreme Optics, Shanxi University, Taiyuan 030006, China

³Department of Physics, University of Michigan, Ann Arbor, Michigan 48109, USA



(Received 14 May 2023; accepted 20 July 2023; published 8 August 2023)

We present precise measurements of the quantum defects of cesium nF_J Rydberg levels. We employ high-precision microwave spectroscopy of $(n+2)D_{5/2} \rightarrow nF_{5/2,7/2}$ transitions for $n = 45$ to 50 in a cold-atom setup. Cold cesium $(n+2)D_{5/2}$ atoms, prepared via two-photon laser excitation, are probed by scanning weak microwave fields interacting with the atoms across the $nF_{5/2,7/2}$ resonances. Transition spectra are acquired using state-selective electric-field ionization and time-gated ion detection. Transition-frequency intervals are obtained by Lorentzian fits to the measured spectral lines, which have linewidths ranging between 70 and 190 kHz, corresponding to about one to three times the Fourier limit. A comprehensive analysis of relevant line-shift uncertainties and line-broadening effects is conducted. We find quantum defect parameters $\delta_0(F_{5/2}) = 0.033\,415\,37(70)$ and $\delta_2(F_{5/2}) = -0.2014(16)$, as well as $\delta_0(F_{7/2}) = 0.033\,564\,6(13)$ and $\delta_2(F_{7/2}) = -0.2052(29)$, for $J = 5/2$ and $7/2$, respectively. Fine-structure parameters A_{FS} and B_{FS} for Cs nF_J are also obtained. Results are discussed in context with previous works, and the significance of the results is discussed.

DOI: [10.1103/PhysRevA.108.022804](https://doi.org/10.1103/PhysRevA.108.022804)

I. INTRODUCTION

Accurate values for energy levels and quantum defects of alkali-metal atoms, including those for high angular momentum states, play an ever-increasing role in testing atomic-structure and quantum-defect theories, as well as in applications such as atomic clocks [1–3], quantum optics [4–6], and Rydberg-atom-based metrology [7,8]. Further, accurate information on atomic levels, atomic interactions, ac shifts, etc., covered in our paper, is important in the design of quantum gates in neutral-atom quantum computing and quantum simulation [9,10]. High-precision microwave spectroscopy is well suited for precise measurement of Rydberg transition frequencies due to long atom-field interaction times and low transition linewidths that can be realized in slowly expanding cold-atom clouds. In combination with effective static-field control to reduce line shifts and broadening, accurate and precise transition-frequency measurements allow for the extraction of atomic constants. This includes the quantum defects of low and high angular momentum Rydberg states, which are affected by short-range many-electron interactions in the ionic Rydberg-atom core as well as long-range dipolar and quadrupolar long-range interaction between valence electron and ionic core, respectively [11]. For alkali-metal Rydberg atoms in high- ℓ ($\ell \geq 3$) states, the quantum defect arises from the ionic-core polarizabilities [12–14] and the fine structure. Precision measurements of high- ℓ quantum defects

therefore allow one to extract core polarizabilities and fine-structure coupling constants, enabling comparison with and validation of advanced atomic-structure calculations [15–19].

Measurements of the quantum defects and ionization energy of cesium date back as far as 1949 [20,21]. Energy levels of Cs have been determined using classical methods such as grating and interference spectroscopy [22], by means of a high-dispersion Czerny-Turner spectrograph and a hollow-cathode discharge [23], and high-resolution Fourier spectroscopy [24]. These measurements were for low principal quantum numbers, n , and had state-of-the-art accuracy at that time. In addition, Doppler-free laser spectroscopy [25–28] has been used to study Cs energy levels. Bjorkholm and Liao [29,30] proposed a method for resonance-enhanced Doppler-free multiphoton excitation, which was experimentally applied by Sansonetti and Lorenzen to measure fine structures for the odd-parity states of Cs. Goy *et al.* [31] have measured quantum defects for S , P , D , and F Rydberg levels of Cs ($23 < n < 45$) by high-resolution double-resonance spectroscopy with an accuracy of about 1 MHz. In 1987, Weber and Sansonetti [32] extensively measured absolute energy levels of Cs $nS_{1/2}$, $nP_{1/2}$, $nD_{5/2}$, $nF_{5/2}$, and $nG_{7/2}$ Rydberg states using nonresonant and resonance-enhanced Doppler-free two-photon spectroscopy and obtained quantum defects. There, the laser wavelengths were measured using high-precision Fabry-Pérot cavities with an uncertainty of 0.0002 cm^{-1} at most levels. These data are being widely used as reference values to this day. Recently, detailed high-resolution-spectroscopy work on nS , nP , and nD cesium Rydberg states has been performed in an ultracold gas [33,34]. Other alkali-metal atoms, such as Rb [14] and K [35], have been researched along similar lines. While many

*ycjiao@sxu.edu.cn

†zhaojm@sxu.edu.cn

‡grathel@umich.edu

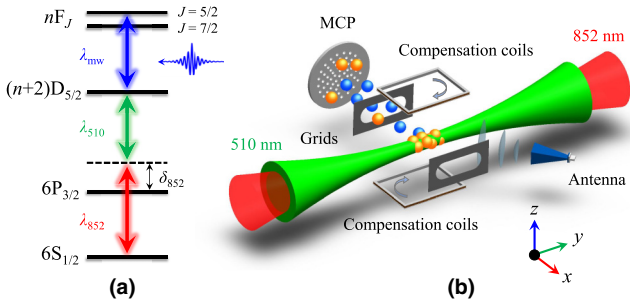


FIG. 1. (a) Level diagram and excitation scheme. The $(n+2)D_{5/2}$ state is resonantly excited by two-photon excitation using $\lambda = 852$ - and 510 -nm laser beams with an intermediate-state detuning of $\delta_{852} = +330$ MHz. Microwaves λ_{mw} drive Rydberg transitions of the type $(n+2)D_{5/2} \rightarrow nF_{5/2,7/2}$. (b) Schematic of the experimental setup (not to scale). The excitation lasers are counterpropagated through the MOT center along the y direction. The microwaves are introduced as shown. The $(n+2)D_{5/2}$ and microwave-excited $nF_{5/2}$ and $nF_{7/2}$ Rydberg atoms are counted by state-selective electric-field ionization and time-gated ion detection with a microchannel plate (MCP) detector. Three pairs of grids and compensation coils are placed on the x , y , and z axes to compensate stray electric and magnetic fields (only one set of each shown). Gold and blue balls represent laser-excited $(n+2)D$ and microwave-coupled nF atoms.

properties of alkali-metal Rydberg atoms are generic, quantitative differences arise from large variations in the specific quantum defects. With regard to the F series, which we focus on here, it is noted that in both Rb and Cs the F quantum defects are small, but in Rb they are about a factor of 2 smaller (≈ 0.017 in Rb versus ≈ 0.034 in Cs).

In the present paper, we laser excite $nD_{5/2}$ Rydberg states of Cs using a two-photon excitation scheme, and perform high-precision microwave spectroscopy of the electric dipole $(n+2)D_{5/2} \rightarrow nF_{5/2,7/2}$ transitions. We describe our experimental procedures in some detail. We then obtain microwave spectra with resonance linewidths ranging between 70 and 190 kHz, and determine transition frequencies with uncertainties of a few kHz. Using the Rydberg-Ritz formula, we extract the quantum defect parameters δ_0 and δ_2 for both fine-structure components $nF_{5/2,7/2}$ of Cs, allowing us to also extract the fine-structure coupling constant, A_{FS} and B_{FS} . Results are discussed in context with previous works.

II. EXPERIMENTAL SETUP

In Fig. 1(a) we display the level diagram used in our experiment. Atoms in $(n+2)D_{5/2}$ states ($n = 45$ – 50) are populated using the displayed two-photon excitation scheme. The intermediate-state detuning of $\delta_{852} = +330$ MHz eliminates photon scattering and radiation pressure. The laser pulses have a duration of 500 ns. The density of the prepared Rydberg-atom sample is $\lesssim 4 \times 10^6 \text{ cm}^{-3}$. Subsequent to laser preparation, a microwave pulse of 20- μs duration is applied to drive a Rydberg transition of the type $(n+2)D_{5/2} \rightarrow nF_{5/2,7/2}$, yielding narrow-linewidth microwave spectra.

Selected details of the experimental setup are shown in Fig. 1(b). Cs ground-state atoms are laser cooled and trapped in a standard magneto-optical trap (MOT) with a temperature

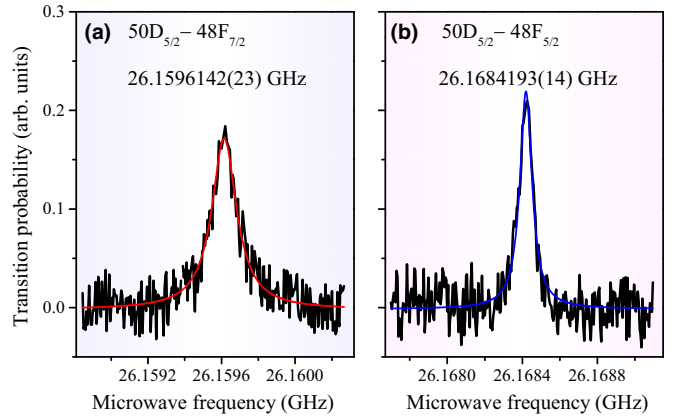


FIG. 2. Measurements of the microwave spectra for the $50D_{5/2}$ to $48F_{7/2}$ transition (a) and $48F_{5/2}$ transition (b). To improve the signal-to-noise ratio, data are averaged over 25 or more repetitions of the experiment. Black lines show the detected Rydberg transition probability signals. Curves in color are Lorentz fits to the spectra, yielding central frequencies of 26.159 614 2(23) GHz and 26.168 419 3(14) GHz, with statistical uncertainties, $\Delta\nu_{\text{stat}}$, in brackets.

$\approx 100 \mu\text{K}$ and a peak density $\approx 10^{10} \text{ cm}^{-3}$. After switching off the MOT and waiting for a delay time of 1 ms, we apply the 852- and 510-nm Rydberg-excitation laser pulses, which have respective Gaussian beam-waist parameters of $w_0 = 750$ and $1000 \mu\text{m}$. Both lasers are external-cavity diode lasers from Toptica that are locked to a high-finesse Fabry-Pérot cavity, resulting in laser linewidths of less than 100 kHz. The microwaves are generated by an analog signal generator (Keysight N5183B, frequency range 9 kHz to 40 GHz), and emitted with an antenna (PASTERNAK WR-34, frequency range 22 to 33 GHz), covering the Cs $(n+2)D_{5/2}$ to nF_J Rydberg series for n ranging from 45 to 50. The microwave output power and frequency scans are controlled with a LABVIEW program. After turning off the microwave field, an electric-field ramp is applied to the grids on the x axis for state-selective field ionization of the Rydberg atoms [11]. Due to their different ionization limits, the laser-prepared $(n+2)D$ and microwave-coupled nF Rydberg atoms result in ion signals at different arrival times on the microchannel plate (MCP) detector, allowing state-selective recording with a boxcar and a data acquisition card. Subsequent data analysis yields spectra as shown in Fig. 2.

Due to large beam waists and small laser intensities, the two-photon optical Rydberg-excitation Rabi frequency is fairly small; it is $\Omega = \Omega_{852}\Omega_{510}/(2\delta_{852}) \approx 2\pi \times 9 \text{ kHz}$. Optical-pumping, saturation-broadening, and radiation-pressure effects on the optical transitions are thus avoided. For our optical-pulse duration of 500 ns, the Rydberg-atom excitation probability per atom is $\approx 2 \times 10^{-4}$. The resultant Rydberg-atom density for a ground-state atom density in the MOT of $\lesssim 10^{10} \text{ cm}^{-3}$ is $\lesssim 4 \times 10^6 \text{ cm}^{-3}$, corresponding to a distance of $\approx 25 \mu\text{m}$ between Rydberg atoms in the sample. As shown in Sec. IV E, this density is sufficiently low that transition shifts due to Rydberg-atom interactions are negligible, as required for high-precision microwave spectroscopy of Rydberg levels.

III. MICROWAVE SPECTROSCOPY

In the experiment, we lock the frequencies of the two excitation lasers for resonant preparation of Rydberg atoms in a $(n+2)D_{5/2}$ ($n=45-50$) state. The microwave frequency is scanned across the $(n+2)D_{5/2} \rightarrow nF_{5/2,7/2}$ transitions, driving the atoms between these states. High-precision microwave spectra of the $(n+2)D_{5/2} \rightarrow nF_{5/2,7/2}$ transitions are then obtained by state-selective field ionization and gated ion detection [11], and subsequent data analysis.

In Fig. 2, we show measured microwave spectra of the $50D_{5/2} \rightarrow 48F_{7/2}$ (a) and $48F_{5/2}$ (b) transitions. The duration of the microwave drive pulses is $20 \mu\text{s}$. Lorentz fits (colored lines in Fig. 2) yield center frequencies of 26.159 614 2(23) and 26.168 419 3(14) GHz for $50D_{5/2} \rightarrow 48F_{7/2}$ and $50D_{5/2} \rightarrow 48F_{5/2}$, respectively, with statistical uncertainties from the fits, $\Delta\nu_{\text{stat}}$, as indicated. Due to the inversion of the fine structure of the Cs nF Rydberg levels, the $48F_{7/2}$ level energy is lower than that of $48F_{5/2}$. The Lorentz fits also yield linewidths of about 163 and 78 kHz for the $48F_{7/2}$ and $48F_{5/2}$ lines, respectively, which is a factor of 1.5 to 3 larger than the Fourier-limited linewidth of 50 kHz for our $20\text{-}\mu\text{s}$ microwave drive pulses. In the following, line broadening and systematic line shifts will be discussed.

IV. SYSTEMATIC EFFECTS

Careful analysis of the uncertainty caused by systematic effects is an important part of precision spectroscopic measurements. In this section, we will analyze our uncertainties, including those arising from the microwave generator, electric, and magnetic fields, as well as Rydberg-atom interactions.

A. Signal generator frequency

To obtain accurate transition-frequency readings, we use an external atomic clock (SRS FS725) as a reference to lock the crystal oscillator of the microwave generator. The clock's relative uncertainty is $\pm 5 \times 10^{-11}$, which results in a frequency deviation of less than 10 Hz [36] for the Rydberg transitions of interest. Hence, systematic shifts due to signal-generator frequency uncertainty are negligible.

B. Background dc magnetic fields

While we carefully zero the magnetic field, an inhomogeneity of $\lesssim 5$ mG is sufficient to cause several tens of kHz of broadening of the $(n+2)D_{5/2} \rightarrow nF_J$ lines. We have confirmed this by simulations of Zeeman spectra, which in the relevant magnetic-field range are in the linear (low- B) regime of the $(n+2)D_{5/2}$ and the nF Rydberg-state fine structures, the Paschen-Back regime of the nF_J hyperfine structure, and the transition regime of the $(n+2)D_{5/2}$ hyperfine structure. Assuming an unpolarized atomic sample and linear field polarizations, the Zeeman broadening is symmetric, consistent with the shapes of both spectral lines in Fig. 2. The unresolved hyperfine structure of the $(n+2)D_{5/2}$ levels, also included in the simulations, may add about 10 kHz to the

measured linewidths. The $(n+2)D_{5/2}$ hyperfine structure is estimated using hyperfine-structure measurements on the $7D_{5/2}$ state [37,38], and applying n^{*-3} scaling (where n^* is the effective quantum number).

In detail, both experimental data and simulations of Zeeman spectra as a function of magnetic compensation fields B_x , B_y , and B_z show symmetric and linear Zeeman splittings, as well as line-broadening effects that are also symmetric about the line centers. We have eliminated the Zeeman splittings and minimized residual magnetic-field-induced line broadening by adjustment of the compensation fields B_x , B_y , and B_z . The remnant magnetic field is estimated to be $\lesssim 5$ mG. The symmetry of the Zeeman spectra about the line centers mostly results from the absence of circular polarization in the atom-field drives. The observed symmetry may be aided by the facts that the atomic sample is unpolarized and that the remnant sub-5-mG fields are likely of quadrupolar character, without a preferred direction within the atomic sample. Based on the symmetry of any residual magnetic-field-induced broadening, as well as the small ($\lesssim 5$ mG) magnitude of any remnant magnetic fields, we assert that systematic magnetic shifts of the reported frequencies of $(n+2)D_{5/2} \rightarrow nF_{5/2,7/2}$ transitions are $\lesssim 1$ kHz. For the Zeeman-shift uncertainty we therefore use 1 kHz. We have verified the dc magnetic-field compensation every day throughout the data taking.

C. Background dc electric fields

Stark effects typically cause asymmetric line broadening and, more importantly, a net line shift. Hence, special attention must be paid to compensating Stark effects. The electric-field compensation process is described in [39]. Here we provide relevant details.

Figure 3 shows the peak shifts of microwave spectra as shown in Fig. 2, for the $50D_{5/2} \rightarrow 48F_{5/2}$ transition, as a function of voltages applied to the compensation electrodes along the x , y , and z directions. Zero shift is marked with a horizontal dashed line that shows the resonant frequency of the $50D_{5/2} \rightarrow 48F_{5/2}$ transition at zero field. Quadratic fits (blue curves) yield the voltages that must be applied to the respective electrodes for optimal dc electric-field compensation (vertical black lines; voltage values with fit uncertainties are provided in the panels). The systematic uncertainty due to dc Stark shifts is estimated by computation of the rms spread of the frequency shifts of the five data points closest to the apex of the three fit functions (red data points). The standard error of the mean of the average of these five points is 0.62 kHz, and the net uncertainty that follows from the uncertainties of the individual data points is 0.7 kHz. As a conservative estimate of $\Delta\nu_{E_{\text{dc}}}$ for the systematic dc Stark shift we therefore use $\Delta\nu_{E_{\text{dc}}} = 1$ kHz. It should be noted that we have verified the dc stray-electric-field compensation on a daily basis in order to maintain optimal compensation throughout the entire data-taking sequence. Using the known polarizability of the transition frequency of $\Delta\alpha \approx 600 \text{ kHz}/(\text{V/m})^2$ (averaged over all values of the magnetic quantum number m_j) and noting that the Stark shift of the transition is $-\alpha E_{\text{dc}}^2/2$, a systematic dc Stark shift of 1 kHz translates into a dc electric-field uncertainty of about 2 mV/m at the location of the atoms.

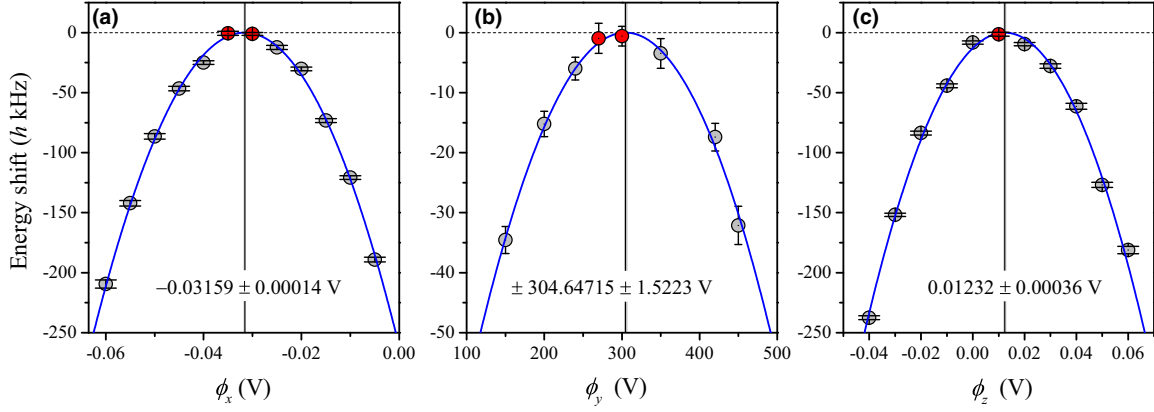


FIG. 3. Measurements of frequency shifts of the $50D_{5/2} \rightarrow 48F_{5/2}$ transition as a function of voltages, ϕ , applied to electric-field compensation electrodes along the (a) x , (b) y , and (c) z direction, respectively. In (a) and (c) we apply the compensation voltage to one electrode, with the matching other connected to or referenced to ground [see Fig. 1(b)]. In (b), we apply the voltage shown to both y electrodes with opposite polarity, with the large overall magnitude of the compensation voltage being due to the large distance and efficient shielding of the y electrodes from the location of the atoms. The data show the expected quadratic Stark shift behavior, which is in good agreement with simulations. The five red data points are used to estimate the systematic dc Stark shift of the transition frequencies reported in our paper.

D. Ac Stark shifts

We next evaluate systematic shifts due to the ac Stark effect. The microwave intensity at the location of the atoms is varied by changing the synthesizer output power. In Figs. 4(a) and 4(b), we display the measured frequency interval as a function of the microwave output power. For the measured frequency interval of the $50D_{5/2} \rightarrow 48F_{7/2}$ transitions in Fig. 4(a) and for microwave power less than $0.5 P_0$, with reference level $P_0 = -50$ dBm on the signal generator, we find that the transition has no observable ac shift. The statistical variation of the line position over this microwave power range is less than ≈ 2 kHz. Here, we may take multiple measurements within this power range and average the results to improve statistics. The data point for the transition frequency in Fig. 4(a) is included in Table I.

For the $50D_{5/2} \rightarrow 48F_{5/2}$ transition in Fig. 4(b) we observe that the microwave power needed to drive the transition is on the order of a factor of 20 larger than for the $50D_{5/2} \rightarrow 48F_{7/2}$ transition. This observation is in line with our computed

microwave Rabi frequencies, which are about a factor of 5 lower for the $50D_{5/2} \rightarrow 48F_{5/2}$ than for the $50D_{5/2} \rightarrow 48F_{7/2}$ transition (averaged over m_j). Hence, we expect that the $50D_{5/2} \rightarrow 48F_{5/2}$ transition requires about a factor of 25 more in power than the $50D_{5/2} \rightarrow 48F_{7/2}$ transition to achieve spectral lines of similar height (as observed in the experiment). In addition, the $50D_{5/2} \rightarrow 48F_{5/2}$ transition has a significant ac shift, which is due to the higher microwave power required to drive that transition, and due to the large matrix element for the perturbing $50D_{5/2} \rightarrow 48F_{7/2}$ transition. Comparing observed and calculated ac shifts, one may use Fig. 4(b) to estimate microwave electric fields and Rabi frequencies. The estimation shows that at a power of $1P_0$ the microwave electric field at the location of the atoms is ≈ 15 mV/m, and the Rabi frequency is on the order of 50 kHz. This estimate accords well with the fact that a microwave power of about $1P_0$ is required to saturate the $50D_{5/2} \rightarrow 48F_{5/2}$ transition with our 20- μ s-long microwave pulses. The lowest microwave fields used to probe the ≈ 25 times stronger $50D_{5/2} \rightarrow 48F_{7/2}$ transition [see Fig. 4(a)] are about ≈ 1 mV/m. Following these consistency checks, we apply a linear fit to the data in Fig. 4(b) to determine the y intercept as our best estimate for the zero-microwave-field transition frequency of the $50D_{5/2} \rightarrow 48F_{5/2}$ transition. In Fig. 4(b) and in analogous data in Table I we report zero-microwave-field transition frequencies and the

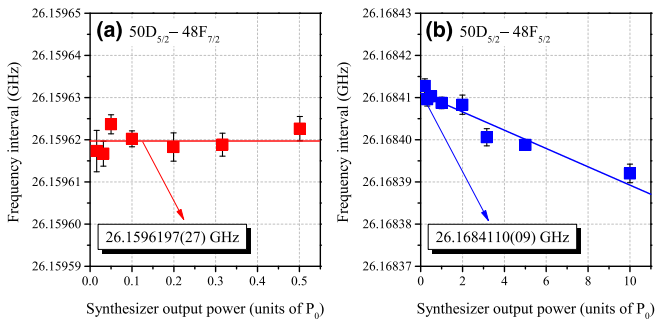


FIG. 4. Frequencies of the $50D_{5/2} \rightarrow 48F_{7/2}$ (a) and $50D_{5/2} \rightarrow 48F_{5/2}$ (b) transitions vs synthesizer output power in units of $P_0 = -50$ dBm. Line centers and their uncertainties are obtained from Lorentzian fits to the microwave spectra. The measurement quantifies the ac shift on both transitions.

TABLE I. Summary of measured transition frequencies (in GHz) and statistical uncertainties of $(n+2)D_{5/2} \rightarrow nF_j$ transitions.

n	$F_{5/2}$	$F_{7/2}$
45	31.7931217(13)	31.7824486(30)
46	29.7532231(13)	29.7432386(39)
47	27.8841485(11)	27.8747898(18)
48	26.1684110(09)	26.1596197(27)
49	24.5906056(37)	24.5823252(16)
50	23.1371463(13)	23.1293529(33)

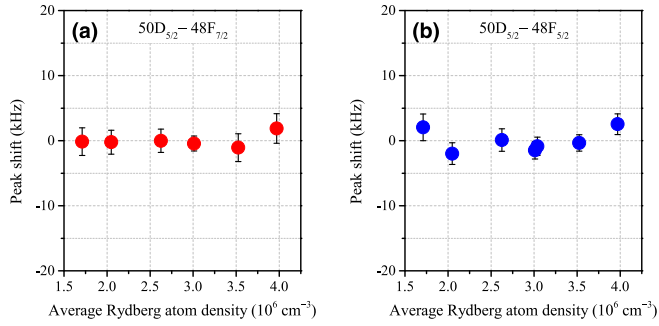


FIG. 5. Line shifts of the $50D_{5/2} \rightarrow 48F_{7/2}$ (a) and $50D_{5/2} \rightarrow 48F_{5/2}$ (b) transitions vs estimated Rydberg-atom density. Line centers and their uncertainties are obtained from Lorentzian fits to the microwave spectra. The measurements show that Rydberg-atom interactions have no measurable effect on the reported transition frequencies.

uncertainties of the y intercepts that result from the linear fits. Hence, the effects of ac Stark shifts are included in the statistical fit uncertainty and do not need to be accounted for separately.

E. Shifts due to Rydberg-atom interactions

Finally we consider the effect of atomic interactions. Rydberg energy levels can be shifted due to a ubiquitous variety of dipolar and higher-order van der Waals interactions [40], which scale as n^{11}/R^6 for the case of second-order dipolar interaction (R is the internuclear separation). However, in the present experiment the dominant interactions arise from the resonant electric dipole coupling between atoms in $(n+2)D_{5/2}$ and nF_J states, which become populated in the course of the optical and microwave excitations. Hence, the leading Rydberg-atom interaction scales as n^4/R^3 . To explore potential transition-frequency shifts from these interactions, we vary the power of the 510-nm Rydberg-excitation laser in order to vary the Rydberg-atom density in the sample. As the optical two-photon excitation is far from saturation, this method presents an efficient means to vary the Rydberg-atom density. We then look for possible line shifts as a function of Rydberg-atom density.

Figures 5(a) and 5(b) show the measured line shift as a function of Rydberg-atom density for the $50D_{5/2} \rightarrow 48F_{7/2}$ and $50D_{5/2} \rightarrow 48F_{5/2}$ transitions, respectively. It can be seen that for estimated Rydberg-atom densities $\lesssim 4 \times 10^6 \text{ cm}^{-3}$, the density-induced line shift is less than the statistical variation of the data points, which is on the order of a few kHz in Fig. 5. Noting that average atom densities are somewhat below estimated peak densities, the internuclear separation between Rydberg atoms is estimated to be $\gtrsim 25 \mu\text{m}$ at the highest densities in Fig. 5.

For a theoretical estimation of the density shifts, as a representative case we have computed binary molecular potentials for various combinations of Rydberg atoms in $50D_{5/2}$ and $48F_J$ states using methods developed in [41,42]. It is found that the leading interaction between pairs of $50D_{5/2}$ -state atoms is a dipolar van der Waals type of interaction, which scales as C_6/R^6 , with a dispersion coefficient of

$C_6 \approx 3.5 \text{ GHz } \mu\text{m}^6$. The leading interaction between pairs of $48F_J$ -state atoms also is a dipolar van der Waals type of interaction, with a dispersion coefficient of $C_6 \approx -20 \text{ GHz } \mu\text{m}^6$. The resultant level shifts at $30 \mu\text{m}$ internuclear separation amount to only tens of Hz and are negligible. Atom pairs in a mix of $50D_{5/2}$ and $48F_J$ states interact much more strongly via resonant dipolar interactions, which scale as C_3/R^3 . Here we find $|C_3| \approx 2.6 \text{ GHz } \mu\text{m}^3$ for $50D_{5/2} + 48F_{7/2}$ pairs, and $|C_3| \approx 0.16 \text{ GHz } \mu\text{m}^3$ for $50D_{5/2} + 48F_{5/2}$ pairs (values averaged over all molecular potentials for the allowed angular-momentum projections onto the internuclear axis). The $|C_3|$ coefficient for $50D_{5/2} + 48F_{7/2}$ is on the order of $(n^* e a_0)^2 / (4\pi \epsilon_0)$, the approximate maximum value for resonant dipolar coupling (n^* is the effective quantum number). The large ratio between the C_3 coefficients for $50D_{5/2} + 48F_{7/2}$ versus $50D_{5/2} + 48F_{5/2}$ is due to angular matrix elements and is related to a likewise difference in Rabi frequency squares for the $50D_{5/2} \rightarrow 48F_J$ microwave transitions studied in our paper. For atom pairs separated at $30 \mu\text{m}$, the magnitudes of the line shifts are about 100 kHz for $50D_{5/2} + 48F_{7/2}$ and about 6 kHz for $50D_{5/2} + 48F_{5/2}$. The 96 dipolar interaction potentials for $50D_{5/2} + 48F_{7/2}$ (and 72 for $50D_{5/2} + 48F_{5/2}$) are nearly symmetric about the asymptotic energies (meaning there are as many attractive as there are repulsive potentials, and the magnitudes of positive and negative C_3 coefficients tend to be equal), and they are fairly evenly spread. For atom pairs separated at $30 \mu\text{m}$, the average line shifts are only 26 Hz for $50D_{5/2} + 48F_{7/2}$ and 150 Hz for $50D_{5/2} + 48F_{5/2}$. Hence, the line shifts due to Rydberg-atom interactions are negligible, and the main effect of the interactions is a line broadening of the $50D_{5/2} \rightarrow 48F_{7/2}$ microwave transition, without causing significant shifts. The simulation results are in line with the experimental observations in Fig. 5, where no density-dependent line shift is measured for either transition. Hence, systematic shifts due to Rydberg-atom interactions are neglected in the present paper.

Summarizing our discussion of systematic shifts, in the following systematic uncertainties of 1 kHz are assumed for each of the dc electric and magnetic shifts. These are added in quadrature to the statistical uncertainties. All other systematic effects are either considerably smaller, or they are already covered by the statistical uncertainty of the measurements. The extra broadening of the $48F_{7/2}$ line in Fig. 2 and in analogous data for other close-by n values is attributed to symmetric shifts due to Rydberg-atom interactions, which affects the $nF_{7/2}$ lines about 20 times more than the $nF_{5/2}$ lines. The dipolar Rydberg-atom interactions have no measurable effect on the line centers, at our level of accuracy. It is noted that the differences in (symmetric) line broadening of the $48F_{7/2}$ and $48F_{5/2}$ lines shown in Fig. 2, as well as similar differences observed for other close-by n values, cannot be attributed to differential effects of residual magnetic fields at the MOT center.

V. RESULTS AND DISCUSSIONS

A. Transition frequencies

We have performed a series of microwave-spectroscopy measurements of $(n+2)D_{5/2} \rightarrow nF_{5/2,7/2}$ transitions for $n = 45\text{--}50$. The extracted transition frequency intervals and

their statistical uncertainties, Δv_{stat} , are listed in Table I. It is seen there that the statistical uncertainties range between 1 and 4 kHz. As discussed in Sec. IV, ac Stark shift uncertainties are included in the statistical uncertainty, Rydberg-density shifts are neglected, and dc electric and Zeeman systematic uncertainties are 1 kHz each. Hence, the net uncertainties, Δv , used below, are given by

$$\Delta v = \sqrt{\Delta v_{\text{stat}}^2 + 2(\text{kHz}^2)}, \quad (1)$$

with Δv_{stat} taken from Table I.

B. Quantum defects of nF_J levels versus n

The transition frequencies from an initial Rydberg state (n, ℓ, J) to a final state (n', ℓ', J') follow:

$$\nu_{n, \ell, J}^{n', \ell', J'} = R_{\text{Cs}} c \left[\frac{1}{(n - \delta_{n, \ell, J})^2} - \frac{1}{(n' - \delta_{n', \ell', J'})^2} \right], \quad (2)$$

$$\Delta \delta_F(n) = \left| \frac{1}{2} s^{-3/2} \right| \sqrt{\left(\frac{\nu}{c R_{\text{Cs}}} \right)^2 \left[\left(\frac{\Delta \nu}{\nu} \right)^2 + \left(\frac{\Delta R_{\text{Cs}}}{R_{\text{Cs}}} \right)^2 \right] + [2(n+2)_D^{*-3} \Delta(n+2)_D^*]^2}. \quad (4)$$

The relative uncertainty of the Rydberg constant for Cs, $\Delta R_{\text{Cs}}/R_{\text{Cs}} = 1.9 \times 10^{-12}$, contributes the least to $\Delta \delta_F$ (and has a negligible effect), followed by the frequency uncertainties of our measurements, $\Delta \nu/\nu$, from Table I and Eq. (1). The uncertainties $\Delta(n+2)_D^*$ of the quantum defects of the $(n+2)D_{5/2}$ states from Table V in [32] are the dominant source of uncertainty of our results for $\delta_F(n)$, listed in Table II.

We see that the measured quantum defects exhibit a significant increase with principal quantum number, n , for both $F_{5/2}$ and $F_{7/2}$. The uncertainties are all the same at the present level of precision because the uncertainties $\Delta(n+2)_D^*$ for the $(n+2)D_{5/2}$ states from [32], derived from the $A = \delta_0$ and $B = \delta_2$ values provided for $D_{5/2}$ in Table V therein, are the dominant source of uncertainty for all measurements made.

C. Quantum defect parameters δ_0 and δ_2 for nF_J

The quantum defect can be written as [11,44]

$$\delta(n) = \delta_0 + \frac{\delta_2}{(n - \delta_0)^2} + \frac{\delta_4}{(n - \delta_0)^4} + \dots \quad (5)$$

TABLE II. Summary of quantum defects, $\delta_F(n)$, and their uncertainties from Eqs. (3) and (4), for $J = 5/2$ and $7/2$.

n	$\delta(F_{5/2})$	$\delta(F_{7/2})$
45	0.03331591(65)	0.03346340(65)
46	0.03331988(65)	0.03346726(65)
47	0.03332401(65)	0.03347137(65)
48	0.03332788(65)	0.03347533(65)
49	0.03333144(65)	0.03347920(65)
50	0.03333469(65)	0.03348245(65)

with initial-state and final-state quantum defects $\delta_{n, \ell, J}$ and $\delta_{n', \ell', J'}$, respectively. There, $c = 2.99792458 \times 10^8$ m/s is the speed of light and $R_{\text{Cs}} = 109736.86273038(21) \text{cm}^{-1}$ is the Rydberg constant for Cs, the uncertainty of which is dominated by the Committee on Data of the International Science Council (CODATA) [43] uncertainty of R_{∞} , with the mass uncertainties of the Cs ion and the electron playing no significant role.

The quantum defects of the nF_J states are then written as

$$\delta_F(n) = n - \left((n+2)_D^{*-2} - \frac{\nu}{c R_{\text{Cs}}} \right)^{-1/2} = n - s^{-1/2}, \quad (3)$$

where $(n+2)_D^*$ is the effective quantum number of the $(n+2)D_{5/2}$ state, taken from [32], and $s = (n+2)_D^{*-2} - \frac{\nu}{c R_{\text{Cs}}}$. From the measured frequency intervals in Table I, ν , we then obtain the quantum defects of nF_J according to Eq. (3). The uncertainties of the measured quantum defects are

where δ_0 and δ_i ($i = 2, 4, \dots$) are the leading and higher-order quantum defect parameters. In general, when $n > 20$, we only consider the first two terms on the right-hand side in Eq. (5).

In Fig. 6, we plot the measured quantum defects δ_F for the nF_J states from Table II versus n^{*-2} . Fits according to Eq. (5) to the data then yield $\delta_0(F_{5/2}) = 0.03341537(70)$ and $\delta_2(F_{5/2}) = -0.2014(16)$ for $nF_{5/2}$, and $\delta_0(F_{7/2}) = 0.0335646(13)$ and $\delta_2(F_{7/2}) = -0.2052(29)$ for $nF_{7/2}$, respectively. The quantum defect parameters δ_0 and

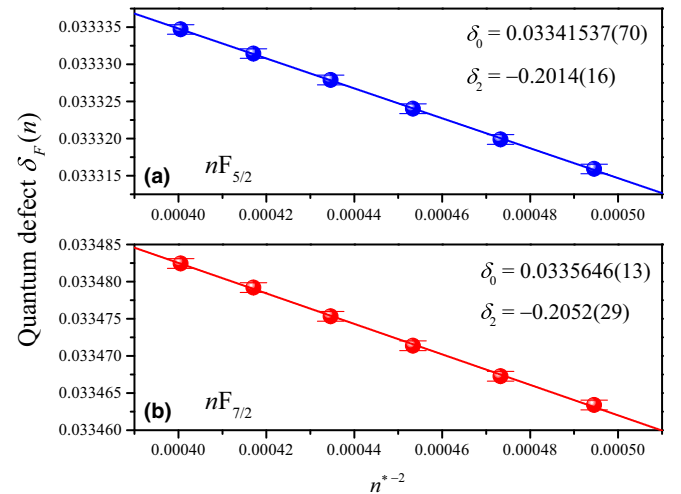


FIG. 6. Measured quantum defects $\delta_F(n)$ of nF_J levels as a function of n^{*-2} for $nF_{5/2}$ (a) and $nF_{7/2}$ (b). The circles and uncertainty bars show the data from Table II. Blue ($nF_{5/2}$) and red ($nF_{7/2}$) solid lines represent fitting results according to Eq. (5), yielding the quantum defect parameters $\delta_0(F_{5/2}) = 0.03341537(70)$ and $\delta_2(F_{5/2}) = -0.2014(16)$, and $\delta_0(F_{7/2}) = 0.0335646(13)$ and $\delta_2(F_{7/2}) = -0.2052(29)$, for $J = 5/2$ and $7/2$, respectively.

TABLE III. Quantum defect parameters δ_0 and δ_2 for nF_J levels from this paper and several previous works [31,32].

	δ_0	δ_2		
$nF_{5/2}$	0.033 415 37(70)	-0.2014(16)	This paper	($45 \leq n \leq 50$)
	0.033392(30)	-0.191(30)	[31]	($23 < n < 45$)
	0.03341424(96)	-0.198674	[32]	($6 < n < 65$)
$nF_{7/2}$	0.033 564 6(13)	-0.2052(29)	This paper	($45 \leq n \leq 50$)
	0.033537(25)	-0.191(20)	[31]	($23 < n < 45$)

δ_2 are listed in Table III. To compare with previous works, we also list the quantum defects for F_J obtained in [31,32]. In [32], the quantum defects were measured using non-resonant and resonantly enhanced Doppler-free two-photon spectroscopy of $nD_{5/2}$, $nF_{5/2}$, etc. There, the level energies were determined directly by measuring laser wavelengths with a high-precision Fabry-Pérot interferometer, which had an uncertainty of 0.0002 cm^{-1} (6 MHz), whereas in [31] quantum defects were obtained by high-resolution double-resonance spectroscopy with n ranging from 23 to 45 in the millimeter-wave domain, with an accuracy of about 1 MHz.

In our paper, we measure the quantum defects of the nF_J states by microwave spectroscopy with a narrow linewidth on the order of 100 kHz, from which accurate Rydberg-level frequency intervals are extracted with an uncertainty of ≈ 2 kHz. Since we have used $nD_{5/2}$ quantum defects from [32] as an input for our analysis, and since their uncertainties are the dominant source of uncertainty in our measurement, unsurprisingly for $nF_{5/2}$ our results in Table III agree within uncertainties with those from [32]; also, the uncertainties are comparable. A main deliverable of our paper consists of a set of quantum defect parameters δ_0 and δ_2 for $nF_{7/2}$, for which [32] has no data. Our quantum defects are more precise than those from [31] by factors of 40 and 20, for $nF_{5/2}$ and $nF_{7/2}$, respectively. The values still agree within the uncertainties stated in [31].

In view of the fact that our uncertainties are dominated by the D quantum defects used as input, we note that D quantum defects from a more recent measurement [34] yield F quantum defects in our analysis that are essentially identical with the ones listed in our Table III, within uncertainties, namely, $\delta_0 = 0.033\ 414\ 53(70)$, $\delta_2 = -0.2012(16)$ for $F_{5/2}$ and $\delta_0 = 0.033\ 563\ 7(13)$, $\delta_2 = -0.2050(29)$ for $F_{7/2}$.

D. Fine-structure intervals for nF_J

The narrow spectral profiles allow us to clearly distinguish the fine structure of the nF Rydberg states for $J = 5/2$ and $7/2$, over our principal quantum number range of $n = 45$ to 50 (limited by the frequency coverage of our microwave source). From the frequency intervals ν for the $(n+2)D_{5/2} \rightarrow nF_J$ transitions in Table I, we obtain the fine-structure splittings of the nF_J levels. In Fig. 7, we display the fine-structure splittings between $nF_{5/2}$ and $nF_{7/2}$ as a function of the effective quantum number n^* . Note that for Cs the nF fine structure is inverted, i.e., $J = 5/2$ is higher in energy than $J = 7/2$. The fine structure, attributed to the spin-orbit interaction of the Rydberg electron, is commonly described in terms of fine-structure coupling constants A_{FS} and B_{FS} [11]. The fine-structure

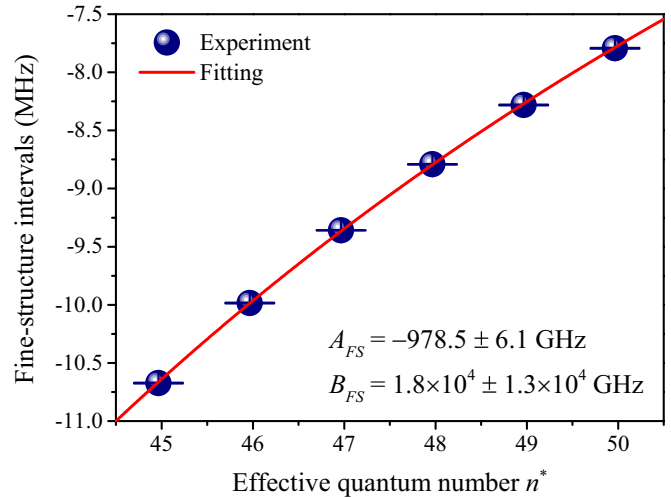


FIG. 7. Measured fine-structure frequency intervals between $nF_{5/2}$ and $nF_{7/2}$ as a function of effective quantum number n^* . The red solid line represents a fit to the expression $A_{FS}n^{*-3} + B_{FS}n^{*-5}$, yielding fine-structure parameters $A_{FS} = -978.5 \pm 6.1$ GHz and $B_{FS} = 1.8 \times 10^4 \pm 1.3 \times 10^4$ GHz, respectively.

splitting is then given by $A_{FS}n^{*-3} + B_{FS}n^{*-5}$. Fitting the data in Fig. 7 with this expression, we find $A_{FS} = -978.5 \pm 6.1$ GHz and $B_{FS} = 1.8 \times 10^4 \pm 1.3 \times 10^4$ GHz. These values are consistent with earlier results [45] within our uncertainties (we did not find an uncertainty in [45]).

VI. CONCLUSION

We have employed microwave spectroscopy and cold-atom methods to obtain the transition frequency intervals of cesium $(n+2)D_{5/2} \rightarrow nF_{5/2,7/2}$ transitions and have extracted quantum defects for the $nF_{5/2,7/2}$ levels. A careful analysis of systematic uncertainties has been conducted. For $nF_{5/2}$, our results and uncertainties agree well with data from [32]. For $nF_{7/2}$, our results are more precise than earlier data from [31] by a factor of about 20. The measured fine-structure intervals have allowed us to also determine the A_{FS} and B_{FS} fine-structure parameters for Cs nF levels; our results agree with previous data from [45] to within our uncertainty.

Our precise study of intrinsic properties of Rydberg atoms, such as quantum defects, is of significance for experimental work that relies on the availability of such data, as well as for theoretical research on the structure of complex atoms, where experimental data are often desired for a test of theoretical methods and results. The uncertainties of our paper were severely limited by the uncertainty of input data used for the quantum defects of our launch states, $nD_{5/2}$. Based upon the frequency uncertainties $\Delta\nu$ we have already achieved in the present paper, we expect that studies based upon alternate transition schemes, which are not reliant on previously measured quantum defects, will allow us to improve our uncertainties for nF_J quantum defects by a factor $\gtrsim 10$. Such methods may also enable studies of higher- ℓ quantum defects as well as refined studies of the hyperfine structure of Rydberg atoms. This may extend to the very small hyperfine structure of Cs nD Rydberg states.

ACKNOWLEDGMENTS

This work is supported by the National Natural Science Foundation of China (Grants No. 61835007, No. 12120101004, No. 62175136, and No. 12241408); the Scientific Cooperation Exchanges Project of Shanxi Province

(Grant No. 202104041101015); the Changjiang Scholars and Innovative Research Team in Universities of the Ministry of Education of China (Grant No. IRT 17R70); and the 1331 project of Shanxi Province. G.R. acknowledges support by the University of Michigan.

-
- [1] B. Bloom, T. Nicholson, J. Williams, S. Campbell, M. Bishof, X. Zhang, W. Zhang, S. Bromley, and J. Ye, An optical lattice clock with accuracy and stability at the 10^{-18} level, *Nature (London)* **506**, 71 (2014).
- [2] K. W. Martin, G. Phelps, N. D. Lemke, M. S. Bigelow, B. Stuhl, M. Wojcik, M. Holt, I. Coddington, M. W. Bishop, and J. H. Burke, Compact Optical Atomic Clock Based on a Two-Photon Transition in Rubidium, *Phys. Rev. Appl.* **9**, 014019 (2018).
- [3] W. R. Milner, J. M. Robinson, C. J. Kennedy, T. Bothwell, D. Kedar, D. G. Matei, T. Legero, U. Sterr, F. Riehle, H. Leopardi, T. M. Fortier, J. A. Sherman, J. Levine, J. Yao, J. Ye, and E. Oelker, Demonstration of a Timescale Based on a Stable Optical Carrier, *Phys. Rev. Lett.* **123**, 173201 (2019).
- [4] B. Zhao, M. Müller, K. Hammerer, and P. Zoller, Efficient quantum repeater based on deterministic Rydberg gates, *Phys. Rev. A* **81**, 052329 (2010).
- [5] T. Wilk, A. Gaëtan, C. Evellin, J. Wolters, Y. Miroshnychenko, P. Grangier, and A. Browaeys, Entanglement of Two Individual Neutral Atoms Using Rydberg Blockade, *Phys. Rev. Lett.* **104**, 010502 (2010).
- [6] L. Isenhower, E. Urban, X. L. Zhang, A. T. Gill, T. Henage, T. A. Johnson, T. G. Walker, and M. Saffman, Demonstration of a Neutral Atom Controlled-NOT Quantum Gate, *Phys. Rev. Lett.* **104**, 010503 (2010).
- [7] J. D. Carter, O. Cherry, and J. D. D. Martin, Electric-field sensing near the surface microstructure of an atom chip using cold Rydberg atoms, *Phys. Rev. A* **86**, 053401 (2012).
- [8] J. Sedlacek, A. Schwettmann, H. Kübler, R. Löw, T. Pfau, and J. P. Shaffer, Microwave electrometry with Rydberg atoms in a vapour cell using bright atomic resonances, *Nat. Phys.* **8**, 819 (2012).
- [9] P. Scholl, M. Schuler, H. J. Williams, A. A. Eberharter, D. Barredo, K.-N. Schymik, V. Lienhard, L.-P. Henry, T. C. Lang, T. Lahaye, A. M. Läuchli, and A. Browaeys, Quantum simulation of 2D antiferromagnets with hundreds of Rydberg atoms, *Nature (London)* **595**, 233 (2021).
- [10] X. Wu, X. Liang, Y. Tian, F. Yang, C. Chen, Y.-C. Liu, M. K. Tey, and L. You, A concise review of Rydberg atom based quantum computation and quantum simulation*, *Chin. Phys. B* **30**, 020305 (2021).
- [11] T. F. Gallagher, *Rydberg Atoms*, Cambridge Monographs on Atomic, Molecular, and Chemical Physics (Cambridge University, New York, 1994).
- [12] M. Born and W. Heisenberg, Über den einfluß der deformierbarkeit der ionen auf optische und chemische konstanten. I, *Z. Phys.* **23**, 388 (1924).
- [13] J. E. Mayer and M. G. Mayer, The polarizabilities of ions from spectra, *Phys. Rev.* **43**, 605 (1933).
- [14] S. J. Berl, C. A. Sackett, T. F. Gallagher, and J. Nunkaew, Core polarizability of rubidium using spectroscopy of the ng to nh , ni Rydberg transitions, *Phys. Rev. A* **102**, 062818 (2020).
- [15] M. S. Safronova, S. G. Porsev, C. Sanner, and J. Ye, Two Clock Transitions in Neutral Yb for the Highest Sensitivity to Variations of the Fine-Structure Constant, *Phys. Rev. Lett.* **120**, 173001 (2018).
- [16] C. Cheung, M. S. Safronova, S. G. Porsev, M. G. Kozlov, I. I. Tupitsyn, and A. I. Bondarev, Accurate Prediction of Clock Transitions in a Highly Charged Ion with Complex Electronic Structure, *Phys. Rev. Lett.* **124**, 163001 (2020).
- [17] M. Kaur, R. Nakra, B. Arora, C.-B. Li, and B. K. Sahoo, Accurate determination of energy levels, hyperfine structure constants, lifetimes and dipole polarizabilities of triply ionized tin isotopes, *J. Phys. B* **53**, 065002 (2020).
- [18] K. Beloy and A. Derevianko, Second-order effects on the hyperfine structure of p states of alkali-metal atoms, *Phys. Rev. A* **78**, 032519 (2008).
- [19] K. Beloy, U. I. Safronova, and A. Derevianko, High-Accuracy Calculation of the Blackbody Radiation Shift in the ^{133}Cs Primary Frequency Standard, *Phys. Rev. Lett.* **97**, 040801 (2006).
- [20] H. R. Kratz, The principal series of potassium, rubidium, and cesium in absorption, *Phys. Rev.* **75**, 1844 (1949).
- [21] J. R. McNally, J. P. Molnar, W. J. Hitchcock, and N. F. Oliver, High members of the principal series in caesium, *J. Opt. Soc. Am.* **39**, 57 (1949).
- [22] H. Kleiman, Interferometric measurements of cesium I, *J. Opt. Soc. Am.* **52**, 441 (1962).
- [23] K. B. S. Eriksson and I. Wenåker, New wavelength measurements in Cs I, *Phys. Scr.* **1**, 21 (1970).
- [24] C. J. Sansonetti, K. L. Andrew, and J. Verges, Polarization, penetration, and exchange effects in the hydrogenlike nf and ng terms of cesium, *J. Opt. Soc. Am.* **71**, 423 (1981).
- [25] C. J. Lorenzen, K. H. Weber, and K. Niemax, Energies of the $n^2s_{1/2}$ and $n^2d_{3/2,5/2}$ states of Cs, *Opt. Commun.* **33**, 271 (1980).
- [26] C. J. Lorenzen and K. Niemax, Non-monotonic variation of the quantum defect in Cs nd_j term series, *Z. Phys. A* **311**, 249 (1983).
- [27] C. J. Lorenzen and K. Niemax, Precise quantum defects of ns , np and nd levels in Cs I, *Z. Phys. A* **315**, 127 (1984).
- [28] M. S. O'Sullivan and B. P. Stoicheff, Doppler-free two-photon absorption spectrum of cesium, *Can. J. Phys.* **61**, 940 (1983).
- [29] J. E. Bjorkholm and P. F. Liao, Line shape and strength of two-photon absorption in an atomic vapor with a resonant or nearly resonant intermediate state, *Phys. Rev. A* **14**, 751 (1976).
- [30] P. F. Liao and J. E. Bjorkholm, Measurement of the Fine-Structure Splitting of the $4f$ State in Atomic Sodium Using Two-Photon Spectroscopy With a Resonant Intermediate State, *Phys. Rev. Lett.* **36**, 1543 (1976).
- [31] P. Goy, J. M. Raimond, G. Vitrant, and S. Haroche, Millimeter-wave spectroscopy in cesium Rydberg states. quantum defects, fine- and hyperfine-structure measurements, *Phys. Rev. A* **26**, 2733 (1982).

- [32] K. H. Weber and C. J. Sansonetti, Accurate energies of ns , np , nd , nf , and ng levels of neutral cesium, *Phys. Rev. A* **35**, 4650 (1987).
- [33] H. Saßmannshausen, F. Merkt, and J. Deiglmayr, High-resolution spectroscopy of Rydberg states in an ultracold cesium gas, *Phys. Rev. A* **87**, 032519 (2013).
- [34] J. Deiglmayr, H. Herburger, H. Saßmannshausen, P. Jansen, H. Schmutz, and F. Merkt, Precision measurement of the ionization energy of Cs I, *Phys. Rev. A* **93**, 013424 (2016).
- [35] M. Peper, F. Helmrich, J. Butscher, J. A. Agner, H. Schmutz, F. Merkt, and J. Deiglmayr, Precision measurement of the ionization energy and quantum defects of ^{39}K I, *Phys. Rev. A* **100**, 012501 (2019).
- [36] K. Moore, A. Duspayev, R. Cardman, and G. Raithel, Measurement of the Rb g -series quantum defect using two-photon microwave spectroscopy, *Phys. Rev. A* **102**, 062817 (2020).
- [37] J. E. Stalnaker, V. Mbele, V. Gerginov, T. M. Fortier, S. A. Diddams, L. Hollberg, and C. E. Tanner, Femtosecond frequency comb measurement of absolute frequencies and hyperfine coupling constants in cesium vapor, *Phys. Rev. A* **81**, 043840 (2010).
- [38] Z. Wang, X. Hou, J. Bai, and J. Wang, Measuring the hyperfine splitting and deriving the hyperfine interaction constants of the cesium $5p^67d^2d_{5/2}$ excited state, *Appl. Sci.* **10**, 8178 (2020).
- [39] J. Bai, S. Bai, X. Han, Y. Jiao, J. Zhao, and S. Jia, Precise measurements of polarizabilities of cesium ns Rydberg states in an ultra-cold atomic ensemble, *New J. Phys.* **22**, 093032 (2020).
- [40] A. Reinhard, T. C. Liebisch, B. Knuffman, and G. Raithel, Level shifts of rubidium Rydberg states due to binary interactions, *Phys. Rev. A* **75**, 032712 (2007).
- [41] X. Han, S. Bai, Y. Jiao, L. Hao, Y. Xue, J. Zhao, S. Jia, and G. Raithel, Cs $62D_J$ Rydberg-atom macrodimers formed by long-range multipole interaction, *Phys. Rev. A* **97**, 031403(R) (2018).
- [42] X. Han, S. Bai, Y. Jiao, G. Raithel, J. Zhao, and S. Jia, Adiabatic potentials of cesium $(nd_j)^2$ Rydberg-Rydberg macrodimers, *J. Phys. B* **52**, 135102 (2019).
- [43] E. Tiesinga, P. J. Mohr, D. B. Newell, and B. N. Taylor, CODATA recommended values of the fundamental physical constants: 2018, *Rev. Mod. Phys.* **93**, 025010 (2021).
- [44] C. J. Lorenzen and K. Niemax, Quantum defects of the $n^2p_{1/2,3/2}$ levels in ^{39}K I and ^{85}Rb I, *Phys. Scr.* **27**, 300 (1983).
- [45] K. Fredriksson, H. Lundberg, and S. Svanberg, Fine- and hyperfine-structure investigation in the 5^2d-n^2f series of cesium, *Phys. Rev. A* **21**, 241 (1980).